

© 2019 by Akshat Puri. All rights reserved.

MEASUREMENT OF ANGULAR AND MOMENTUM DISTRIBUTIONS OF CHARGED
PARTICLES WITHIN AND AROUND JETS IN Pb+Pb AND $p\bar{p}$ COLLISIONS AT
 $\sqrt{S_{NN}} = 5.02$ TeV WITH ATLAS AT THE LHC

BY

AKSHAT PURI

DISSERTATION

Submitted in partial fulfillment of the requirements
for the degree of Doctor of Philosophy in Physics
in the Graduate College of the
University of Illinois at Urbana-Champaign, 2019

Urbana, Illinois

Doctoral Committee:

Professor Matthias Grosse Perdekamp, Chair
Professor Anne Marie Sickles, Advisor
¹ Professor Lance Cooper
Professor Bryce Gadaway

Abstract

² Studies of the fragmentation of jets into charged particles in heavy-ion collisions can help in understanding
³ the mechanism of jet quenching by the hot and dense matter created in such collisions, the quark-gluon
⁴ plasma. This thesis presents a measurement of the angular distribution of charged particles around the jet
⁵ axis as measured in Pb+Pb and pp collisions collided at a center of mass energy of $\sqrt{s_{NN}} = 5.02$ TeV. The
⁶ measurement is done using the ATLAS detector at the Large Hadron Collider, and utilizes 0.49 pb^{-1} of
⁷ Pb+Pb and 25 pb^{-1} of pp data collected in 2015. The measurement is performed for jets reconstructed
⁸ with the anti- k_t algorithm with radius parameter $R = 0.4$, and is extended to regions outside the jet cone.
⁹ Results are presented as a function of Pb+Pb collision centrality, and both jet and charged-particle transverse
¹⁰ momenta. It was observed that in Pb+Pb collisions there is a broadening of the jet for charged particles with
¹¹ $p_T < 4 \text{ GeV}$, along with a narrowing for charged particles with $p_T > 4 \text{ GeV}$. Ratios between the angular
¹² distributions in Pb+Pb and pp showed an enhancement for particles with $p_T < 4 \text{ GeV}$ in Pb+Pb collisions,
¹³ with the enhancement increasing up to 2 for $r < 0.3$, and remaining constant for $0.3 < r < 0.6$. Charged
¹⁴ particles with $p_T > 4 \text{ GeV}$ show a small enhancement in the jet core for $r < 0.05$, with a growing suppression
¹⁵ of up to 0.5 for $r < 0.3$ in Pb+Pb collisions. The depletion remains constant for $0.3 < r < 0.6$.

For my Mother, Father, and Brother

Contents

18	Chapter 1 Major Jet Measurements	1
19	1.1 Dijet Balance: x_J	1
20	1.2 Modification of jet yields: R_{AA}	2
21	1.3 Jet Fragmentation	5
22	1.4 Effective Quenching	5
23	1.5 Jet Fluid model	9
24	1.6 Hybrid Model	13

Chapter 1

Major Jet Measurements

This chapter shall discuss some important experimental jet measurements that motivate the study of the main analysis in this thesis. These include the study of the jet yields, dijet asymmetry, and jet fragmentation. It shall then go on to discuss a few models that have been used to explain the data, looking in particular at the following: Effective Quenching (EQ), Soft Collinear Effective Theory (SCET), Hybrid Model, and Jet Fluid Model.

1.1 Dijet Balance: x_J

This section will discuss the dijet balance for $R = 0.4$ jets as measured by ATLAS detector for Pb+Pb collisions at $\sqrt{s_{\text{NN}}} = 2.76$ TeV [1]. The dijet imbalance can be expressed in terms of x_J defined as

$$x_J = \frac{p_{\text{T}2}}{p_{\text{T}1}} \quad (1.1)$$

where $p_{\text{T}2}$ and $p_{\text{T}1}$ are the transverse momenta of the two highest- p_{T} jets in the event respectively. The minimum $p_{\text{T}2}$ considered is 25 GeV and the pair of jets are separated by $|\Delta\phi| > 7\pi/8$. The dijet yields normalized by the number of jets and determined as $1/N_{\text{jets}} dN/dx_J$ are presented as a function of x_J for different centrality intervals, as well as different ranges for $p_{\text{T}1}$. The measured distributions are further unfolded to remove detector resolution effects and allow comparison to theoretical models.

Figure 1.1 shows the x_J distribution for dijet pairs in pp and Pb+Pb collisions in two different centrality bins and two $p_{\text{T}1}$ ranges. It can be seen that the dijet yields in pp are peaked at unity and become narrower for larger $p_{\text{T}1}$ ranges. This reflects the fact that the effects of jet quenching are minimal and the higher- p_{T} jets are better balanced. The dijet yields in peripheral Pb+Pb collisions are similar to the distributions from the pp data, showing that the effects of quenching are smaller. On the other hand, dijet yields in central Pb+Pb collisions are significantly broadened, reflecting the maximal of jet quenching. This is consistent with the picture of the individual jets in the dijet pair traversing different lengths in the QGP and hence losing

46 different amounts of energy. In fact, the distribution for Pb+Pb data is peaked at $x_J = 0.5$, implying a loss
 47 of 50% of the jet p_T .

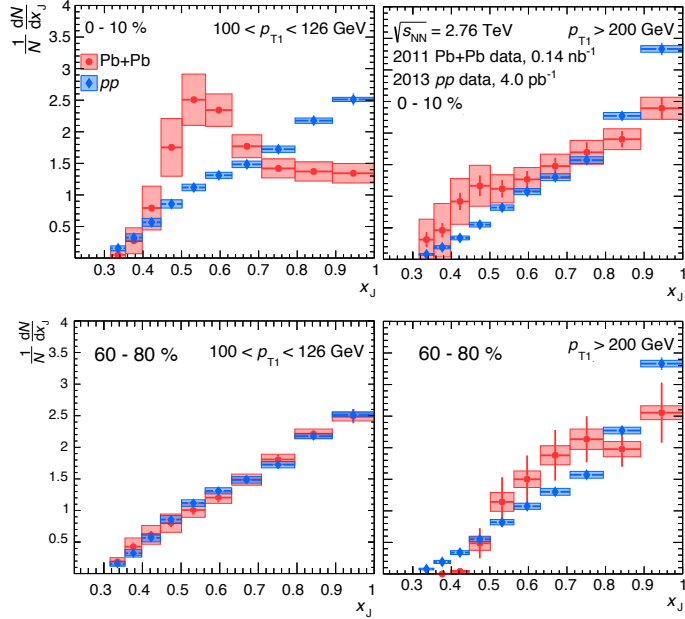


Figure 1.1: The $1/N_{\text{jets}} dN/dx_J$ distributions for $R = 0.4$ jets as a function of x_J for pp (blue) and Pb+Pb (red) collisions. The different panels are for (top) central and (bottom) peripheral collisions in (left) $100 < p_{T1} < 126 \text{ GeV}$ and (right) $p_{T1} > 200 \text{ GeV}$. The pp data is the same in all panels. The statistical uncertainties are indicated by the bars while the boxes indicate the systematic uncertainties. Figures taken from [1]

48 Further measurements of $R = 0.3$ jets are shown in Figure 1.2. These distributions are significantly flatter
 49 than the ones for $R = 0.4$ jets, an observation that is consistent with the expectation that the transverse
 50 momenta correlation between the dijet pair is weaker for jets with smaller radii due to radiation that is
 51 outside the nominal jet cone.

52 1.2 Modification of jet yields: R_{AA}

53 This section discusses the measurement of the inclusive jet R_{AA} as measured by the ATLAS detector for
 54 $R = 0.4$ jets in $\sqrt{s_{\text{NN}}} = 5.02 \text{ TeV}$ Pb+Pb collisions [2].

55 While a measurement that compares the jets in a dijet system to each other as discussed in Section 1.1
 56 can provide valuable information about how jets lose energy, it has the following limitation: If both jets lose
 57 equal amounts of energy, the dijet yield will still be peaked at unity and no new information will be obtained.
 58 Thus, it is useful to compare the jet yields directly between the pp and Pb+Pb systems and construct the jet
 59 R_{AA} observable. This is defined as:

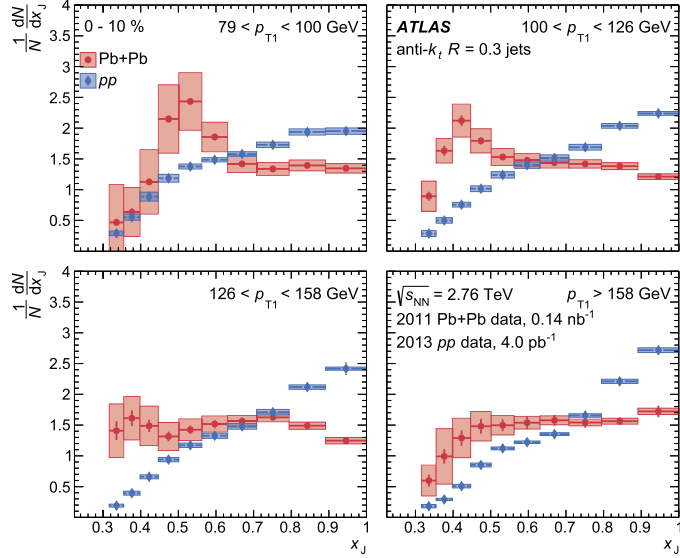


Figure 1.2: The $1/N_{\text{jets}} dN/dx_J$ distributions for $R = 0.3$ jets as a function of x_J in pp and central $\text{Pb}+\text{Pb}$ collisions. The different panels are for different, p_{T1} ranges (top left to bottom right) central and (bottom) peripheral collisions. The $\text{Pb}+\text{Pb}$ data is in red circles while the pp data is in blue diamonds and is the same in all panels. The statistical uncertainties are indicated by the bars while the boxes indicate the systematic uncertainties. Figures taken from [1]

$$R_{\text{AA}} = \frac{\frac{1}{N_{\text{evt}}} \left. \frac{d^2 N_{\text{jet}}}{dp_{\text{T}} dy} \right|_{\text{cent}}}{\langle T_{\text{AA}} \rangle \left. \frac{d^2 \sigma_{\text{jet}}}{dp_{\text{T}} dy} \right|_{\text{pp}}} \quad (1.2)$$

where T_{AA} is the nuclear thickness function and accounts for the geometric enhancement between pp and $\text{Pb}+\text{Pb}$ as discussed in Section ?? and [3].

This measurement was conducted for jets in the 40–1000 GeV range in different rapidity and centrality intervals. The jet yields in pp and $\text{Pb}+\text{Pb}$ collisions are shown in Figure 1.3. The $\text{Pb}+\text{Pb}$ jet yields are scaled by the thickness function and are shown for 8 centrality intervals.

Figure 1.4 shows the measured inclusive jet R_{AA} as a function of jet p_{T} for different centrality bins and jet rapidity $|y| < 2.8$. It can be seen that the most central collisions show a clear suppression with an $R_{\text{AA}} \approx 0.45$ at jet $p_{\text{T}} = 100$ GeV. The R_{AA} value slowly evolves with jet p_{T} and rises to 0.6 at jet $p_{\text{T}} = 800$ GeV. This modification becomes smaller for more peripheral collisions.

The smooth centrality dependence can be more clearly seen in Figure 1.6(a), where R_{AA} is shown as a function of $\langle N_{\text{part}} \rangle$ for jets in the 100–126 GeV and 200–251 GeV ranges. The magnitude of the suppression is also seen to significantly depend on jet p_{T} for $\langle N_{\text{part}} \rangle \geq 50$.

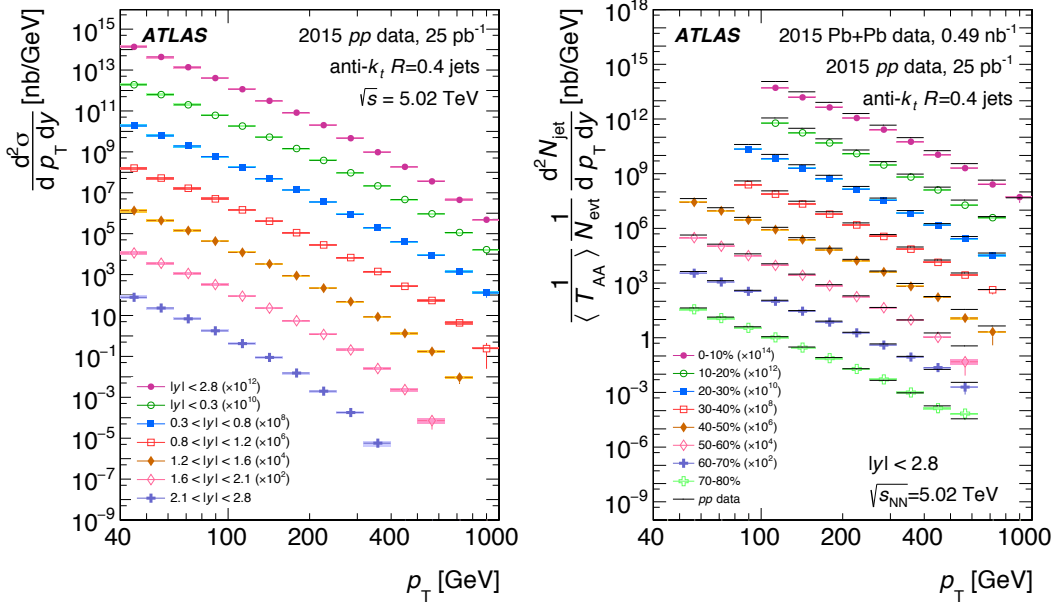


Figure 1.3: (Left) The inclusive jet cross section in pp collisions as a function of jet p_T in different $|y|$ intervals scaled by successive powers of 10^2 for visibility. (Right) Per event inclusive jet yield in $Pb+Pb$ collisions normalized by $\langle T_{AA} \rangle$ as a function of jet p_T in different centrality intervals scaled by successive powers of 10^2 for visibility. The solid lines represent the cross section from pp data at the same rapidity interval scaled by the same 10^2 factor. Figure taken from [2]

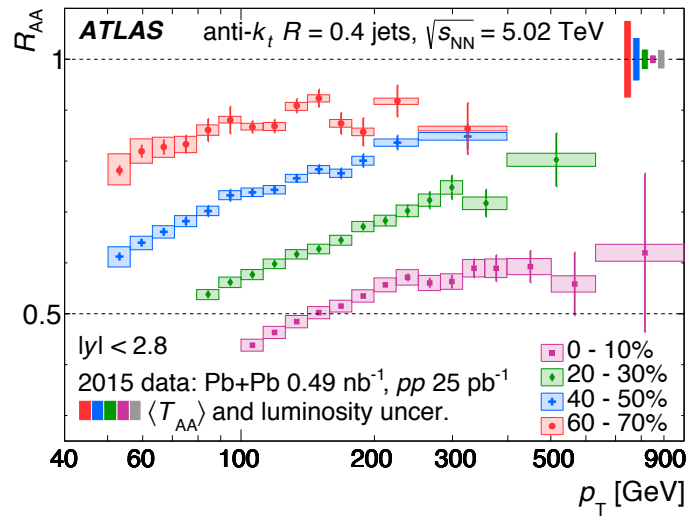


Figure 1.4: The R_{AA} distributions as a function of jet p_T for different centrality bins and jet rapidity $|y| < 2.8$. The error bars represent statistical uncertainties while the shaded boxes represent systematic uncertainties. Figure taken from [2]

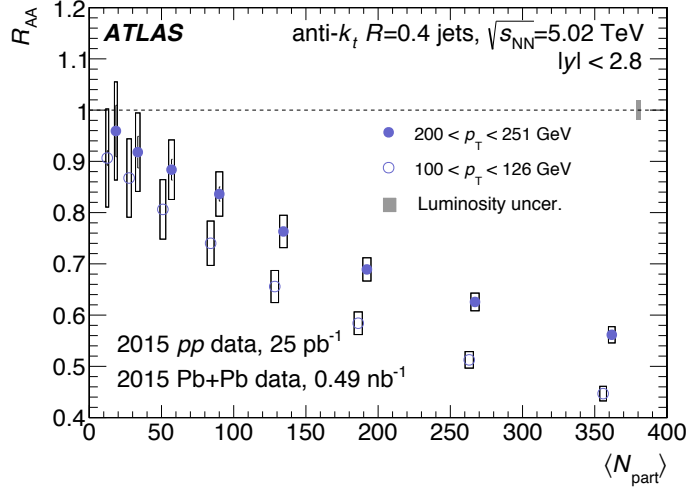


Figure 1.5: The R_{AA} distributions as a function of jet p_T for different centrality bins and jet rapidity $|y| < 2.8$. The error bars represent statistical uncertainties while the shaded boxes represent systematic uncertainties. Figure taken from [2]

72 1.3 Jet Fragmentation

73 [4]

74 1.4 Effective Quenching

75 This discussion is based on the model introduced in Ref. [5]. This phenomenological model emphasizes
 76 the jet p_T dependence of the quark to gluon fraction and the difference between quark-jet and gluon-jet
 77 quenching. It uses an “extended” power law parameterization of the high- p_T hadron spectra coupled with a
 78 quenching that is based on a non-constant fractional energy loss. This model considers the different color
 79 charges carried by quarks and gluons and their different splitting functions, and assumes that gluon jets lose
 80 energy at a rate 9/4 times higher than quark jets. The key assumption of the model are:

- 81 • The energy lost by a jet is radiated at large angles and does not appear within the jet cone. This is
 82 backed by [6].
- 83 • The fragmentation pattern of the jet is unaffected by the presence of the QGP i.e. they fragment as
 84 they would in a vacuum. This is motivated by the idea that the QGP is unable to resolve the internal
 85 jet structure and is supported by [7, 8].

86 The model uses the following extended power-law parameterization to describe the high- p_T jet spectra:

$$\frac{dn}{dp_T^{\text{jet}}} = A \left(\frac{p_{T0}}{p_T^{\text{jet}}} \right)^{n + \beta \log(p_T^{\text{jet}}/p_{T0})} \quad (1.3)$$

where p_{T0} is a reference transverse momentum at which $A = dn/dp_T^{\text{jet}}$, β is the logarithmic derivative of dn/dp_T^{jet} at $p_T^{\text{jet}} = p_{T0}$. Then considering the different quark and gluon fractions as f_{q0} and $f_{g0} = 1 - f_{q0}$ respectively, the combined spectrum for quarks and gluons can be written as:

$$\frac{dN}{dp_T^{\text{jet}}} = A \left[f_{q0} \left(\frac{p_{T0}}{p_T^{\text{jet}}} \right)^{n_q + \beta_q \log(p_T^{\text{jet}}/p_{T0})} + (1 - f_{q0}) \left(\frac{p_{T0}}{p_T^{\text{jet}}} \right)^{n_g + \beta_g \log(p_T^{\text{jet}}/p_{T0})} \right] \quad (1.4)$$

$$f_q(p_T^{\text{jet}}) = \frac{1}{1 + \left(\frac{1 - f_{q0}}{f_{q0}} \right) \left(\frac{p_{T0}}{p_T^{\text{jet}}} \right)^{\Delta n + \Delta \beta \log(p_T^{\text{jet}}/p_{T0})}} \quad (1.5)$$

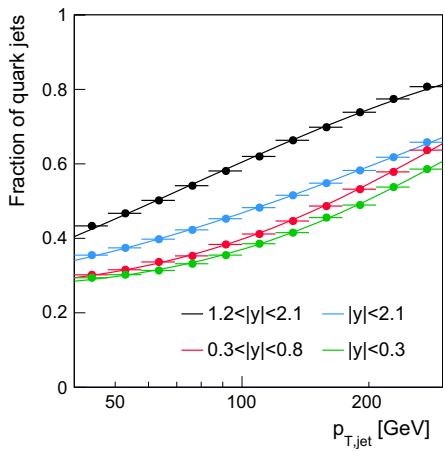
where $\Delta n = n_g - n_q$ and $\Delta \beta = \beta_g - \beta_q$. The p_T dependence of the quark fraction along with the fit is shown in Figure 1.6(a). The fragmentation functions can also be determined using final-state charged hadrons within a $R = 0.4$ jet cone. These are fit to the form $D(z)$, with fits for the quark and gluon fragmentation shown in Figure 1.6(b).

$$D(z) = a \times \frac{(1 + dz)^b}{(1 + ez)^c} \times e^{-fz} \quad (1.6)$$

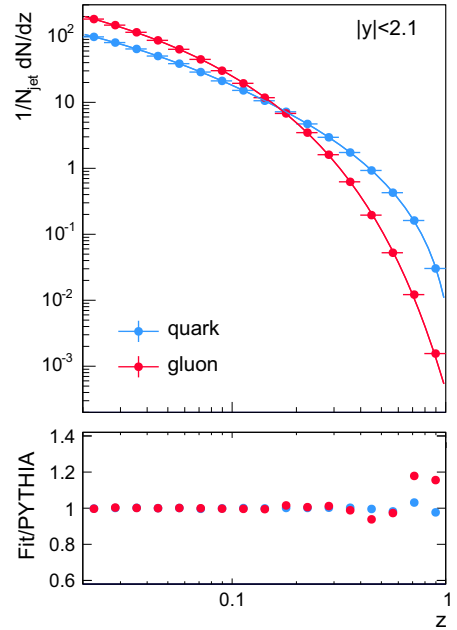
For the quenched spectra, this model assumes a non-constant fractional shift given below as S . This approach is based on [9] and is used because of the inability of the constant fractional shift to explain the jet p_T dependence of measured R_{AA} .

$$S = s' \left(\frac{p_T^{\text{jet}}}{p_{T0}} \right)^\alpha \quad (1.7)$$

where α is an undetermined parameter and s' is the shift for a jet with $p_T^{\text{jet}} = p_{T0}$. This gives the following quenched high- p_T hadron spectra:



(a) The jet quark fraction as a function of p_T^{jet} in different rapidity bins. The points are from PYTHIA8 simulations and the lines are fits to Equation 1.5.



(b) A comparison of the PYTHIA8 quark and gluon fragmentation functions. The solid lines are the fits from The jet quark fraction as a function of p_T^{jet} in different rapidity bins. The points are from PYTHIA8 simulations and the lines are fits to Equation 1.6.

Figure 1.6: Fits to quark fractions and fragmentation functions from PYTHIA8. Figure taken from [5]

$$\frac{dN_Q}{dp_T^{\text{jet}}} = A \left[f_{q0} \left(\frac{p_{T0}}{p_T^{\text{jet}} + S_q} \right)^{n_q + \beta_q \log((p_T^{\text{jet}} + S_q)/p_{T0})} \left(1 + \frac{dS_q}{dp_T^{\text{jet}}} \right) \right. \\ \left. + (1 - f_{q0}) \left(\frac{p_{T0}}{p_T^{\text{jet}} + S_g} \right)^{n_g + \beta_g \log((p_T^{\text{jet}} + S_g)/p_{T0})} \left(1 + \frac{dS_g}{dp_T^{\text{jet}}} \right) \right] \quad (1.8)$$

99 Where the $(1 + dS/dp_T^{\text{jet}})$ term is a Jacobian to preserve the number of jets. Then the R_{AA} can be written as:

$$R_{\text{AA}} = f_q \left(\frac{1}{1 + S_q/p_T^{\text{jet}}} \right)^{n_q + \beta_q \log((p_T^{\text{jet}} + S_q)/p_{T0})} \frac{p_{T0}}{p_T^{\text{jet}}} \left(1 + \frac{dS_q}{dp_T^{\text{jet}}} \right) \times \\ (1 - f_q) \left(\frac{1}{1 + S_g/p_T^{\text{jet}}} \right)^{n_g + \beta_g \log((p_T^{\text{jet}} + S_g)/p_{T0})} \frac{p_{T0}}{p_T^{\text{jet}}} \left(1 + \frac{dS_g}{dp_T^{\text{jet}}} \right) \quad (1.9)$$

(1.10)

100 where the flavor fraction is given by Equation 1.5. These can be fit to the measured ATLAS R_{AA} data as
101 shown in Figure 1.8(a) and the parameters s' and α can be extracted as shown in Figure 1.7.

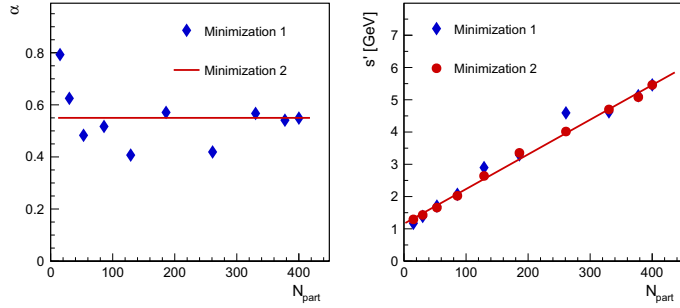
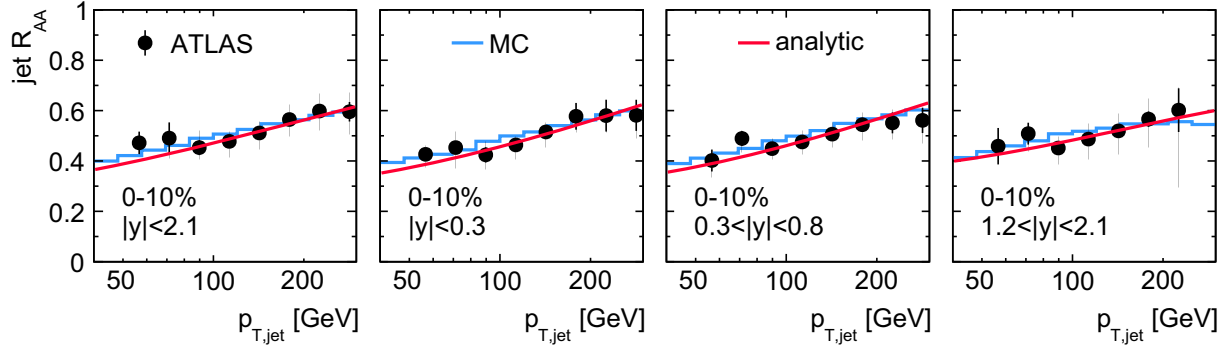
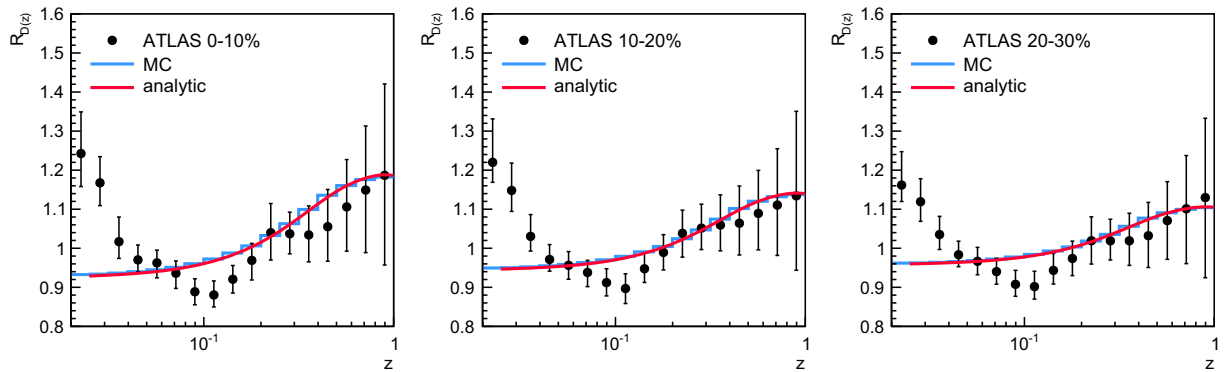


Figure 1.7: The extracted values of α and s' as a function of N_{part} . The first minimization shows fluctuations for α around 0.55, which was then fixed for the second minimization to give an s' that linearly depends on N_{part} . Figure taken from [5]

102 It can be seen that the analytic fits and the MC are in good agreement. While the fits agree with the data
103 by definition, the robustness of the model can be seen in that it describes the data with a single value for α
104 and a simple centrality dependent shift constant s' . Fits to the $D(z)$ distributions are shown in Figure 1.8(b)
105 and it can be seen that while the MC and analytic calculation agree well with each other, they are only
106 able to qualitatively capture some features of the data. The enhancement at high z can be explained by an
107 increased quark content of the jet spectrum and subsequent differential quenching for quark and gluon jets.



(a) A comparison of the R_{AA} as measured by ATLAS for central Pb+Pb collisions in [10], a MC calculation (blue) and the analytic calculation (red) in the EQ model with the extended power-law parameterization and a non-constant fractional energy loss. The different panels are different rapidity intervals.



(b) A comparison of the $R_{D(z)}$ as measured by ATLAS in [11], a MC calculation (blue) and the analytic calculation (red) in the EQ model with the extended power-law parameterization and a non-constant fractional energy loss. The different panels are different centrality intervals.

Figure 1.8: A comparison of measured data, MC, and the analytic calculation of the EQ model. Figure taken from [5]

108 The low z enhancement on the other hand can be considered to be a result of a gluon radiation within the
 109 jet or a wake from the medium itself.

110 1.5 Jet Fluid model

111 This discussion is based on the model introduced in Ref. [12]. This model considers the evolution of the jet
 112 and QGP in a coupled manner, considering the energy and transverse momentum exchange between them.
 113 In this picture, both the jet and medium are allowed to modify each other; the jet is modified via collisional
 114 and radiative processes while the medium evolves hydrodynamically and is modified because it picks up the
 115 energy lost by the jet.

116 The time evolution of the jet is given

$$f_i(\omega_i, k_{\text{T}i}^2, t) = \frac{dN_i(\omega_i k_{\text{T}i}^2, t)}{d\omega_i dk_{\text{T}i}^2} \quad (1.11)$$

117 where i is the type of parton, ω_i is its energy, and k_{T}^2 is its transverse momentum with respect to the jet axis.

118 Then the transport equations can be written in terms of :

$$\frac{df_j}{dt} = e_j \frac{\partial f_j}{\partial \omega_j} + \frac{1}{4} \hat{q}_j \nabla_{k_{\text{T}}}^2 f_j \quad (1.12)$$

$$+ \sum_i \int d\omega_i dk_{\text{T}i}^2 \frac{d\tilde{\Gamma}_{i \rightarrow j}}{d\omega_j dk_{\text{T}j}^2 dt} f_i \quad (1.13)$$

$$- \sum_i \int d\omega_i dk_{\text{T}i}^2 \frac{d\tilde{\Gamma}_{j \rightarrow i}}{d\omega_i dk_{\text{T}i}^2 dt} f_i \quad (1.14)$$

$$(1.15)$$

119 where the first term is the collisional energy loss, the second term is the transverse momentum broadening,
120 and the last two terms are the medium induced gain and loss radiative processes respectively. The splitting
121 processes are given by:

$$\frac{d\Gamma_{i \rightarrow j}}{d\omega_j dk_{\text{T}j}^2 dt} = \frac{2\alpha_S}{\pi} \hat{q}_g \frac{x P_{i \rightarrow j}(x)}{\omega_j k_{\text{T}j}^4} \sin^2 \left(\frac{t - t_i}{2\tau_f} \right) \quad (1.16)$$

122 where $P_{i \rightarrow j}$ is the vacuum splitting function for $i \rightarrow j$ with ω_j being the energy of the radiated parton, τ_f is
123 the formation time of the radiated parton, and $k_{\text{T}j}$ is the transverse momentum of the radiated parton with
124 respect to the parent parton. These transport Equations 1.12 can be solved numerically and agree with R_{AA}
125 measurements [10, 13, 14]. The effects of the medium are included by considering the energy-momentum
126 conservation of the jet-QGP system $\partial_\mu [T_{\text{QGP}}^{\mu\nu} + T_{\text{jet}}^{\mu\nu}] = 0$. Then the source term $J^\nu(x)$ that describes the
127 energy transfer between the jet and the medium can be defined as $J^\nu(x) \equiv -\partial_\mu T_{\text{jet}}^{\mu\nu}$, making the QGP
128 evolution being given by

$$\partial_\mu T_{\text{QGP}}^{\mu\nu} = j^\nu \quad (1.17)$$

129 which characterizes the energy-momentum transfer between the jet and the QGP.

130 An important component of this model is the flow induced by jets. A snapshot of this is shown in
 131 Figure 1.9, where the evolution of the energy density of the medium can be seen in a sample event. A single
 132 jet travels through the QGP, and can be clearly seen in the lower panels after the energy of the medium has
 133 been subtracted out. The V shaped feature seen is the mach cone that is induced by the parton as it moves
 134 faster than the medium sound velocity.

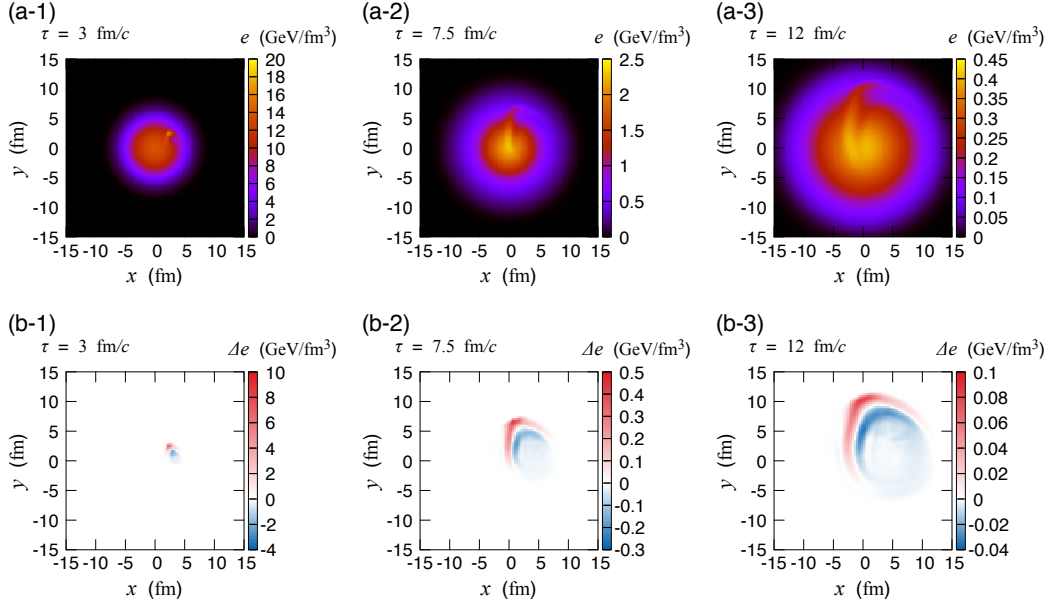


Figure 1.9: (Top) The time evolution of the energy density of the quark gluon plasma with a jet propagating through it. (Bottom) The time evolution of the energy density in the event after the energy density of the QGP has been subtracted out. Figure taken from [12].

135 The final jet energy has two components: the jet shower, and the hydrodynamic response. The former
 136 as discussed above comprises of the collisional energy loss, momentum broadening, and medium induced
 137 radiation. The latter includes the energy lost from the jet shower that thermalizes into the medium and
 138 induces conical flow, some of which is still in the jet cone. This compensates some of the energy lost in the
 139 shower and can be seen in Figure 1.10. While the absolute amount of energy lost increases as a function of
 140 initial jet energy, the fractional energy loss decreases. Furthermore there is a cone size dependence once the
 141 hydrodynamic contributions are included. This is a result of the jet being highly collimated, such that while
 142 an increase in the size does not change the energy much, it does affect the hydrodynamic contribution from
 143 the medium.

144 The R_{AA} distributions constructed with this model and compared to data from CMS [13] are shown in
 145 Figure 1.11. Including the hydrodynamic contribution decreases the energy loss, hence increasing the R_{AA}

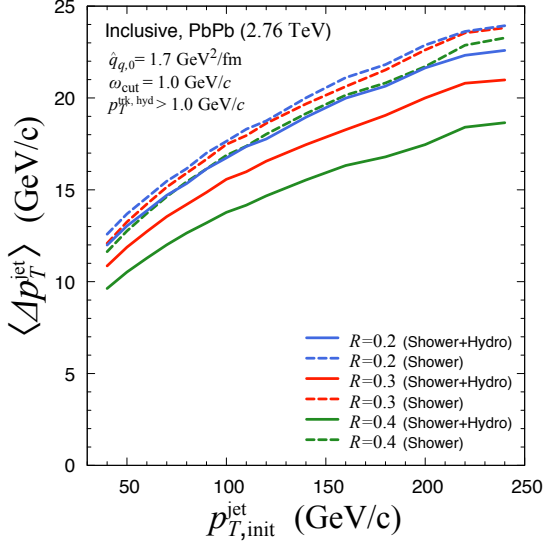


Figure 1.10: (Top) The energy lost by a jets of different radii as a function of their initial energy in central Pb+Pb collisions at $\sqrt{s_{\text{NN}}} = 2.76 \text{ TeV}$. Figure taken from [12].

¹⁴⁶ value and inducing a cone size dependence to the R_{AA} .

¹⁴⁷ The internal structure of the jet, i.e. how energy is spread within it, can be investigated using the jet
¹⁴⁸ shape variable, defined as a per-jet quantity as:

$$\rho_{\text{jet}} = \frac{1}{N_{\text{jet}}} \sum_{\text{jet}} \left[\frac{1}{p_{\text{T}}^{\text{jet}}} \frac{\sum_{\text{trk}} p_{\text{T}}^{\text{ch}}}{\delta r} \right] \quad (1.18)$$

¹⁴⁹ where the sum is over all jets and for all tracks around a jet in an annulus with mean radius r from the jet
¹⁵⁰ axis. The modification in the jet structure then can be defined as:

$$R_{\text{AA}}^\rho = \frac{\rho_{\text{AA}}(r)}{\rho_{\text{pp}}(r)} \quad (1.19)$$

¹⁵¹ A comparison of the jet shape variable ρ and its modification R_{AA}^ρ to data measured by CMS is shown in
¹⁵² Figure 1.12. The individual shower and hydro contributions are seen in Figure 1.12(a). These indicate that
¹⁵³ the shower contribution to the jet shape variable falls steeply as a function of distance from the jet axis
¹⁵⁴ while the hydro contribution is fairly constant at large distances. This is because the energy loss from the
¹⁵⁵ shower is carried away by the jet induced flow to large angles. The R_{AA}^ρ distribution in Figure 1.12(b), shows
¹⁵⁶ that the core is largely unmodified while the outer part of the jet is broadened. The hydro-contribution

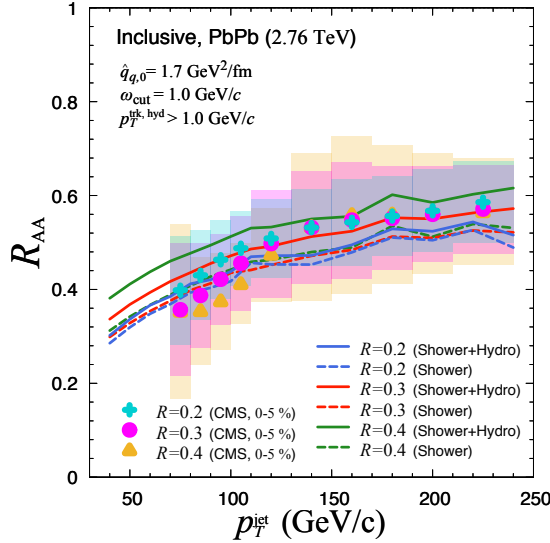


Figure 1.11: The nuclear modification factor R_{AA} as a function of jet p_T as determined by the Jet-Fluid model and compared to the data measured by CMS [13]. The different colors represent different sized jets, with the dashed lines showing the modeled R_{AA} without the hydro-contribution. There is good agreement within the large uncertainties in the data. Figure taken from [12].

¹⁵⁷ mainly has an effect at larger distances from the jet axis. This is consistent with the cone-size dependence
¹⁵⁸ seen in Figure 1.10.

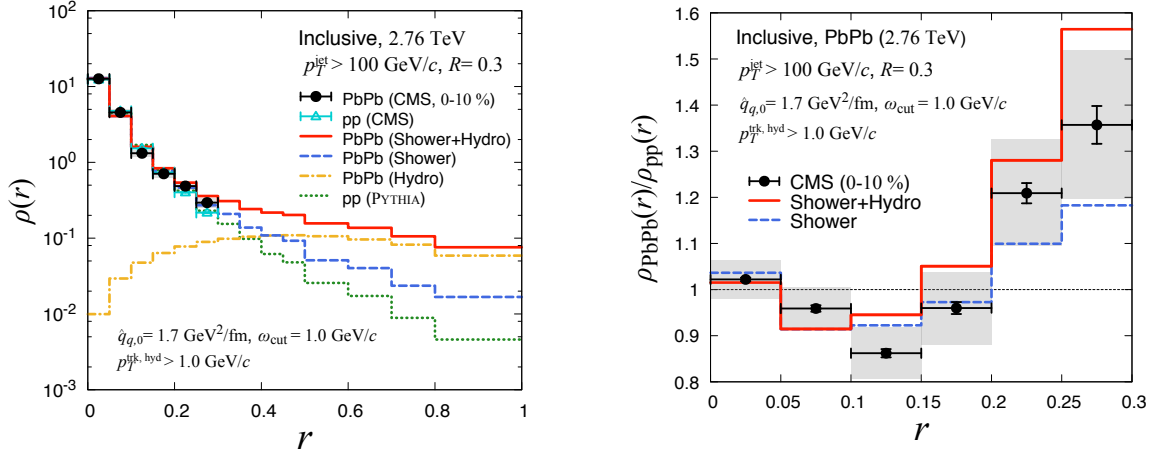
¹⁵⁹ 1.6 Hybrid Model

¹⁶⁰ This discussion is based on the work in Refs. [16–18] and describes jet quenching using a hybrid strong/weak
¹⁶¹ model. It uses perturbative QCD to describe the weakly coupled hard process of jet production and
¹⁶² holographic calculations of the energy loss of energetic probes to model the strong coupling between the
¹⁶³ probe and the plasma [19, 20]. This is a combination of approaches that focus on the following extreme limits:
¹⁶⁴ a weakly coupled system at unrealistically high temperatures that can be treated perturbatively [21, 22] and
¹⁶⁵ a system where the coupling constant is large at all energy scales and Gauge/string duality is applicable [23].

¹⁶⁶ In this model, the jet evolves in space time with the lifetime of the parton in the shower being given by
¹⁶⁷ [24].

$$\tau = 2 \frac{E}{Q^2} \quad (1.20)$$

¹⁶⁸ where Q is its virtuality and E its energy. This evolution is unaffected before the proper time at which the



(a) The jet shape as measured by CMS for pp and central $Pb+Pb$ collisions [15] compared to the Jet Fluid model. The shower (blue) and hydro (orange) contributions to the jet shape are highlighted.

(b) The modification of the jet shape between pp and $Pb+Pb$ as measured by CMS [15] and compared to the Jet Fluid model. The dashed line shows the modeled modification without the hydro-contribution.

Figure 1.12: Fits to CMS data. Figures taken from [12].

169 plasma hydrodynamizes, $\tau_{\text{hydro}} = 0.6$ fm. After this time, the jet-plasma interaction comes into play and the
 170 fragments evolve with the energy loss as:

$$\frac{1}{E_{\text{in}}} \frac{dE}{dx} = -\frac{4}{\pi} \frac{x^2}{x_{\text{stop}}^2} \frac{1}{\sqrt{x_{\text{stop}}^2 - x^2}} \quad (1.21)$$

171 where E_{in} is the initial energy of the parton prior to any quenching and x_{stop} is its stopping distance (jet
 172 thermalization distance). The stopping distance can be written as:

$$x_{\text{stop}} = \frac{1}{2\kappa_{\text{sc}}} \frac{E_{\text{in}}^{1/3}}{T^{4/3}} \quad (1.22)$$

173 where κ_{sc} is a dimensionless free parameter associated to the strong coupling and is used to fit to the
 174 data. The energy loss is characterized by the strong x^2 dependence for $x \ll x_{\text{stop}}$. Furthermore, when x is
 175 comparable to x_{stop} , dE/dx depends nontrivially on E_{in} and x , diverging for $x \rightarrow x_{\text{stop}}$ and $E \rightarrow 0$. The
 176 shower is then embedded into a hydrodynamic description of the QGP from Ref. [25], and the energy loss
 177 expressions are integrated for each parton, from the time it is produced to the time that it splits. The
 178 splitting probabilities are taken to be independent of the medium, depending only on the initial energy of the
 179 daughter partons. These further lose energy as they propagate through the QGP and split. Then the total

180 energy lost by a parton is dependent on the history of splitting and propagation of its parents, grandparents
 181 and so on and so forth.

182 The partons further experience kicks transverse to their direction of motion, a phenomena called transverse
 183 momentum broadening. This effect is mainly experienced by softer partons that are much more affected
 184 by the angular narrowing effects of energy loss, making most measured observables insensitive to the size
 185 of this kick. This is directly related to wider jets losing more energy than narrower ones. The wake left
 186 in the medium from the partons depositing momentum in the QGP as they propagate through it lends a
 187 non-trivial impact to the model predictions. This wake moves in the direction of the jet and is impossible to
 188 separate out in experiments, making its inclusion to any model vital. This wake results in a perturbation
 189 to the hydrodynamic background, resulting in corrections to the final state hadron spectra. This effect is
 190 particularly important for jet substructure observables like jet fragmentation and jet shapes [18].

191 A screening effect recently included in the hybrid model is based on the resolving power of the QGP [26].
 192 As seen in Figure 1.13, the QGP will only resolve daughter partons of a splitting after they are separated by
 193 a certain distance L_{res} . It is only when the partons are resolved that they will be allowed them to lose energy
 194 independent of each other. This delayed quenching results in an enhancement of softer partons at larger
 195 angles from the jet axis compared to the case where the daughter partons are resolved immediately after
 196 they split from the parent parton. This L_{res} has the constraint $1/(\pi T) < L_{\text{res}} < 2/(p_{\text{T}}T)$ based on the Debye
 197 screening length for the plasma, i.e. the length at which the QGP is able to resolve and screen color charges.

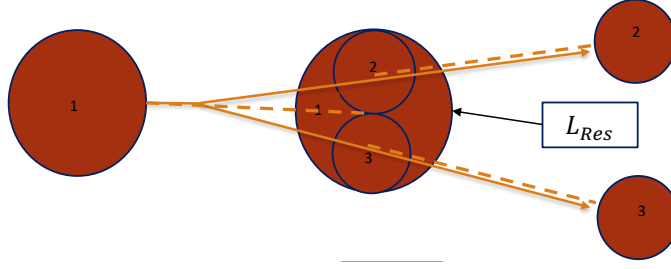


Figure 1.13: A schematic illustrating the resolving power of the QGP. The daughter partons 2 and 3 that come from 1 need to be separated by L_{res} before they are treated individually by the plasma. Prior to that separation, they are treated as one effective parton. Figure taken from [26].

198 The free parameter κ_{sc} is determined by fitting to jet R_{AA} data from CMS [13] as shown in Figure 1.14.
 199 It can be seen that including the L_{res} parameter does not really affect the jet R_{AA} prediction. It is more
 200 interesting to note the R_{AA} dependence on the size of the jet radius, with wider jets losing more energy as
 201 expected.

202 Fixing the κ_{sc} parameter allows for predictions of jet fragmentation. A comparison of the measured and

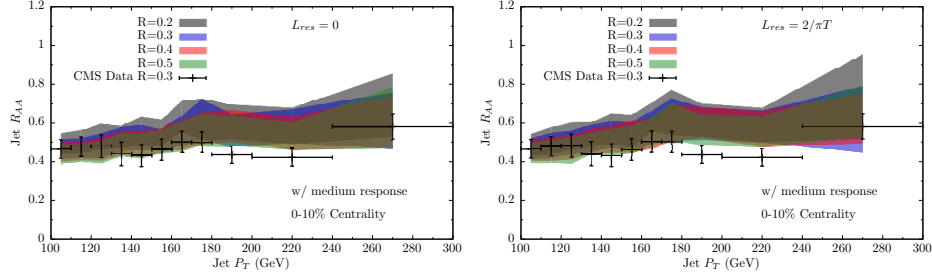


Figure 1.14: The hybrid model without (left) and with (right) the L_{res} parameter, compared to the jet R_{AA} as a function of jet p_{T} in two centrality intervals as measured in Ref. [13]. The different colors correspond to different jet radii. The Hybrid Model is fit to the 100–110 GeV point from the data, giving rise to the colored bands. Figure taken from [26].

203 modeled values of the ratio between jet fragmentation functions in the pp and $\text{Pb}+\text{Pb}$ systems are shown in
 204 Figure ??.

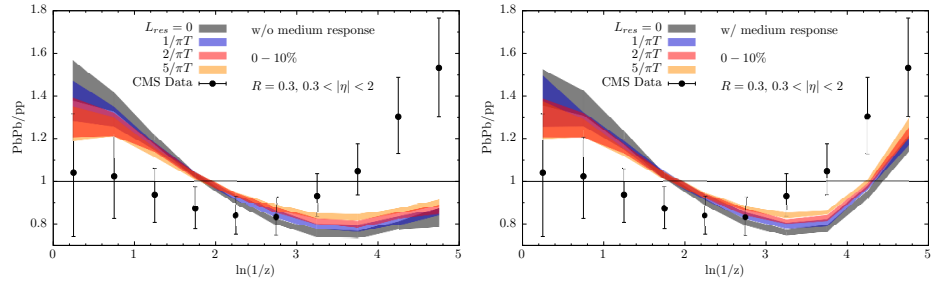


Figure 1.15: The modification to the jet fragmentation from pp to $\text{Pb}+\text{Pb}$ as a function of $\ln(1/z)$ as measured in Ref. [13] compared to the predictions of the hybrid model. The predictions are shown without (left) and with (right) the wake from the QGP responding to the jet. The different colors correspond to different L_{res} parameters. Figure taken from [26].

205 Then the model can be used to predict the R_{AA} dependence on the collision energy, jet p_{T} , and centrality
 206 and is compared to measurements done by ATLAS, ALICE, and STAR [14, 28, 29].

207 While the perturbative evolution of vacuum jet showering is dictated by the Dokshitzer-Gribov-Lipatov-
 208 Altarelli-Parisi (DGLAP) equation, the presence of a medium adds soft non-perturbative behavior.

209 . and processes are and considers strong-weak that the QGP is only able to resolve the products of a parton
 210 splitting after they are separated by a distance L_{res} . This is done in the context of a hybrid string/weak
 211 coupling model of jet quenching, with the resolution parameter resulting in a delayed quenching for partons
 212 with intermediate p_{T} , causing an excess of final state hadrons carrying transverse momenta in the several
 213 GeV range. This effect is seen in the modifications of the jet shapes and jet fragmentation functions,

Bibliography

- 214 [1] ATLAS Collaboration, *Measurement of jet p_T correlations in $Pb+Pb$ and pp collisions at $\sqrt{s_{NN}} = 2.76$*
215 *TeV with the ATLAS detector*, Phys. Lett. **B774** (2017) 379, arXiv: [1706.09363 \[hep-ex\]](#) (cit. on
216 pp. [1–3](#)).
- 217 [2] ATLAS Collaboration, *Measurement of the nuclear modification factor for inclusive jets in $Pb+Pb$*
218 *collisions at $\sqrt{s_{NN}} = 5.02$ TeV with the ATLAS detector*, Phys. Lett. **B790** (2019) 108, arXiv: [1805.05635 \[nucl-ex\]](#) (cit. on pp. [2, 4, 5](#)).
- 220 [3] M. L. Miller, K. Reygers, S. J. Sanders and P. Steinberg, *Glauber Modeling in High-Energy Nuclear*
221 *Collisions*, Annual Review of Nuclear and Particle Science **57** (2007) 205 (cit. on p. 3).
- 222 [4] ATLAS Collaboration, *Measurement of jet fragmentation in $Pb+Pb$ and pp collisions at $\sqrt{s_{NN}} = 5.02$*
223 *TeV with the ATLAS detector*, Phys. Rev. **C98** (2018) 024908, arXiv: [1805.05424 \[nucl-ex\]](#) (cit. on
224 p. [5](#)).
- 225 [5] M. Spousta and B. Cole, *Interpreting single jet measurements in $Pb + Pb$ collisions at the LHC*, Eur.
226 Phys. J. C **76** (2016) 50, arXiv: [1504.05169 \[hep-ph\]](#) (cit. on pp. [5, 7–9](#)).
- 227 [6] CMS Collaboration, *Observation and studies of jet quenching in $PbPb$ collisions at nucleon-nucleon*
228 *center-of-mass energy = 2.76 TeV*, Phys. Rev. **C84** (2011) 024906, arXiv: [1102.1957 \[nucl-ex\]](#)
229 (cit. on p. [5](#)).
- 230 [7] J.-P. Blaizot, E. Iancu and Y. Mehtar-Tani, *Medium-induced QCD cascade: democratic branching and*
231 *wave turbulence*, Phys. Rev. Lett. **111** (2013) 052001, arXiv: [1301.6102 \[hep-ph\]](#) (cit. on p. [5](#)).
- 232 [8] J. Casalderrey-Solana, Y. Mehtar-Tani, C. A. Salgado and K. Tywoniuk, *New picture of jet quenching*
233 *dictated by color coherence*, Phys. Lett. **B725** (2013) 357, arXiv: [1210.7765 \[hep-ph\]](#) (cit. on p. [5](#)).
- 234 [9] R. Baier, Y. L. Dokshitzer, A. H. Mueller and D. Schiff, *Quenching of hadron spectra in media*, JHEP
235 **09** (2001) 033, arXiv: [hep-ph/0106347 \[hep-ph\]](#) (cit. on p. [6](#)).

- [10] ATLAS Collaboration, *Measurements of the Nuclear Modification Factor for Jets in Pb+Pb Collisions at $\sqrt{s_{NN}} = 2.76$ TeV with the ATLAS Detector*, Phys. Rev. Lett. **114** (2015) 072302, arXiv: [1411.2357 \[hep-ex\]](#) (cit. on pp. 9, 10).
- [11] ATLAS Collaboration, *Measurement of inclusive jet charged-particle fragmentation functions in Pb+Pb collisions at $\sqrt{s_{NN}} = 2.76$ TeV with the ATLAS detector*, Phys. Lett. B **739** (2014) 320, arXiv: [1406.2979 \[hep-ex\]](#) [hep-ex] (cit. on p. 9).
- [12] Y. Tachibana, N.-B. Chang and G.-Y. Qin, *Full jet in quark-gluon plasma with hydrodynamic medium response*, Phys. Rev. C **95** (2017) 044909, arXiv: [1701.07951 \[nucl-th\]](#) (cit. on pp. 9, 11–14).
- [13] CMS Collaboration, *Measurement of inclusive jet cross sections in pp and PbPb collisions at $\sqrt{s_{NN}} = 2.76$ TeV*, Phys. Rev. C **96** (2017) 015202, arXiv: [1609.05383 \[nucl-ex\]](#) [nucl-ex] (cit. on pp. 10, 11, 13, 15, 16).
- [14] ALICE Collaboration, *Measurement of charged jet suppression in Pb-Pb collisions at $\sqrt{s_{NN}} = 2.76$ TeV*, JHEP **03** (2014) 013, arXiv: [1311.0633 \[nucl-ex\]](#) [nucl-ex] (cit. on pp. 10, 15).
- [15] CMS Collaboration, *Modification of jet shapes in PbPb collisions at $\sqrt{s_{NN}} = 2.76$ TeV*, Phys. Lett. B **730** (2014) 243, arXiv: [1310.0878 \[nucl-ex\]](#) [nucl-ex] (cit. on p. 14).
- [16] J. Casalderrey-Solana et al., *A Hybrid Strong/Weak Coupling Approach to Jet Quenching*, JHEP **10** (2014) 019, arXiv: [1405.3864 \[hep-ph\]](#) (cit. on p. 13).
- [17] Z. Hulcher et al., *Resolution effects in the hybrid strong/weak coupling model*, Journal of High Energy Physics **2018** (2018) 10, ISSN: 1029-8479 (cit. on p. 13).
- [18] J. Casalderrey-Solana et al., *Angular Structure of Jet Quenching Within a Hybrid Strong/Weak Coupling Model*, JHEP **03** (2017) 135, arXiv: [1609.05842 \[hep-ph\]](#) (cit. on pp. 13, 15).
- [19] P. M. Chesler and K. Rajagopal, *On the Evolution of Jet Energy and Opening Angle in Strongly Coupled Plasma*, JHEP **05** (2016) 098, arXiv: [1511.07567 \[hep-th\]](#) (cit. on p. 13).
- [20] P. M. Chesler and K. Rajagopal, *Jet quenching in strongly coupled plasma*, Phys. Rev. D **90** (2014) 025033, arXiv: [1402.6756 \[hep-th\]](#) (cit. on p. 13).
- [21] P. Jacobs and X.-N. Wang, *Matter in extremis: Ultrarelativistic nuclear collisions at RHIC*, Prog. Part. Nucl. Phys. **54** (2005) 443, arXiv: [hep-ph/0405125 \[hep-ph\]](#) (cit. on p. 13).
- [22] A. Majumder and M. Van Leeuwen, *The Theory and Phenomenology of Perturbative QCD Based Jet Quenching*, Prog. Part. Nucl. Phys. **66** (2011) 41, arXiv: [1002.2206 \[hep-ph\]](#) (cit. on p. 13).

- 265 [23] J. Casalderrey-Solana, H. Liu, D. Mateos, K. Rajagopal and U. A. Wiedemann, *Gauge/String Duality,*
 266 *Hot QCD and Heavy Ion Collisions*, (2011), arXiv: [1101.0618 \[hep-th\]](#) (cit. on p. 13).
- 267 [24] J. Casalderrey-Solana, J. G. Milhano and P. Quiroga-Arias, *Out of Medium Fragmentation from*
 268 *Long-Lived Jet Showers*, *Phys. Lett.* **B710** (2012) 175, arXiv: [1111.0310 \[hep-ph\]](#) (cit. on p. 13).
- 269 [25] T. Hirano, P. Huovinen and Y. Nara, *Elliptic flow in Pb+Pb collisions at $\sqrt{s_{NN}} = 2.76 \text{ TeV}$: hybrid*
 270 *model assessment of the first data*, *Phys. Rev.* **C84** (2011) 011901, arXiv: [1012.3955 \[nucl-th\]](#) (cit. on
 271 p. 14).
- 272 [26] Z. Hulcher et al., *Resolution Effects in the Hybrid Strong/Weak Coupling Model*, (2017), arXiv:
 273 [1707.05245 \[hep-ph\]](#) (cit. on pp. 15, 16).
- 274 [27] CMS Collaboration, *Nuclear modification factor of high transverse momentum jets in PbPb collisions*
 275 *at $\sqrt{s_{NN}} = 2.76 \text{ TeV}$* , 2012, URL: <http://cds.cern.ch/record/1472722>.
- 276 [28] ATLAS Collaboration, *Measurement of the jet radius and transverse momentum dependence of inclusive*
 277 *jet suppression in lead-lead collisions at $\sqrt{s_{NN}} = 2.76 \text{ TeV}$ with the ATLAS detector*, *Phys. Lett.* **B719**
 278 (2013) 220, arXiv: [1208.1967 \[hep-ex\]](#) (cit. on p. 15).
- 279 [29] J. Rusnak, *Inclusive spectrum of charged jets in central Au+Au collisions at $\sqrt{s_{NN}} = 200 \text{ GeV}$ by*
 280 *STAR*, *PoS EPS-HEP2013* (2013) 191 (cit. on p. 15).